IEEE Access
Multidisciplinary ⋮ Rapid Review ⋮ Open Access Journal

Received 16 December 2023, accepted 30 December 2023, date of publication 11 January 2024, date of current version 22 January 2024.

Digital Object Identifier 10.1109/ACCESS.2024.3353041

RESEARCH ARTICLE

Analysis and Design of an Electric Machine Employing a Special Stator With Phase Winding Modules and PMs and a Reluctance Rotor

CHANDRA SEKHAR GOLI[1], (Graduate Student Member, IEEE), MURAT GURHAN KESGIN[2], (Graduate Student Member, IEEE), PENG HAN[3], (Senior Member, IEEE), DAN M. IONEL[2], (Fellow, IEEE), SOMASUNDARAM ESSAKIAPPAN[1], (Senior Member, IEEE), JAMES GAFFORD[4], (Senior Member, IEEE), AND MADHAV D. MANJREKAR[1], (Senior Member, IEEE)

[1]Department of Electrical and Computer Engineering, The University of North Carolina at Charlotte, Charlotte, NC 28223, USA
[2]Spark Laboratory, ECE Department, University of Kentucky, Lexington, KY 40506, USA
[3]Ansys Inc., Irvine, CA 92602, USA
[4]Energy Production and Infrastructure Center, The University of North Carolina at Charlotte, Charlotte, NC 28223, USA

Corresponding author: Chandra Sekhar Goli (cgoli@uncc.edu)

This work was supported by the Vehicle Technologies Office, U.S. Department of Energy, under Award DE-EE0008871.

ABSTRACT This paper introduces a new motor design for traction applications that achieves high power density and meets the power density target of 50kW/L target set by the US Department of Energy. The proposed motor has a doubly salient structure with concentrated toroidal 3-phase windings and permanent magnets (PMs) in the stator and a reluctance rotor, improves torque capability and operating speed compared to traditional designs. A design optimization process was conducted to balance efficiency, power density, and power factor. An equivalent circuit in the DQ reference frame is introduced to enable vector control for the proposed special double salient machine. The resulting design was validated through the creation of an open frame lab prototype (OFLP) and an experimental dyno test bench was developed. The prototype was tested through open circuit tests, static torque tests, and unity power factor tests. This paper also discusses the use of synchronous reference frame theory and per-phase diagrams to calculate electric machine parameters. In addition to experimentation, 3D and 2D electromagnetic FEA simulations have been performed for unity power factor operation as a generator to numerically separate the power loss components.

INDEX TERMS Permanent magnet synchronous motor, PMSM, flux switching machine, FSPM, DQ equivalent circuit, vector control, electric vehicles, EV, traction, propulsion.

I. INTRODUCTION

A special double salient machine having a high volumetric power density of 50kW/L had been proposed in [1] can deliver higher torque and power over a wide speed range of up to 37,500 RPM. This motor has been designed to meet ambitious power density target of 50kW/L set by the U.S. Department of Energy for the year 2025 [2]. The power densities of existing traction motors employed in commercial electric vehicles were significantly below the key targets as reported in [3], [4], and [5]. The proposed special double salient machine in [1] was realized from the concept of parallel path magnetic technology in [6] and [7]. The proposed machine has circumferential flux pattern which was different from traditional doubly-salient permanent magnet machine (DSPM) in [8] and [9] and flux switching permanent magnet machine (FSPM) in [10], [11], and [12]. The PMs in the proposed special machine can be cooled easily by employing

The associate editor coordinating the review of this manuscript and approving it for publication was R. K. Saket.

© 2024 The Authors. This work is licensed under a Creative Commons Attribution-NonCommercial-NoDerivatives 4.0 License.
For more information, see https://creativecommons.org/licenses/by-nc-nd/4.0/

TABLE 1. Nomenclature.

$B_{PM}(\phi,t)$	Air-gap flux density distribution produced by PMs only	ω	Electrical frequency of winding currents
$B_{AR}(\phi,t)$	Air-gap flux density distribution produced by the armature windings solely	φ_a and ϕ_{a0}	Phase angle and angle from the reference axis to the phase-A winding axis
$B_R(\phi,t), B_t(\phi,t)$	Radial and tangential air-gap flux densities	T_{em}	Electromagnetic torque
F_{PM}	Amplitude of the square-wave MMF created by PMs	W_{co}	Co-energy
Λ	Air-gap permeance, the subscripts "max" and "min" of which denote the maximum and minimum value, respectively	f_r, f_t	Radial and tangential components of the electromagnetic stress in the airgap
p_m	Principal pole pairs of the PM array, which was half of the number of PMs	i_a, i_b, i_c, and I_m	Three phase winding currents and Peak value of phase current
p_a	Principal pole pairs of the armature winding, which is the same as the number of coils per phase	W_{max}	Peak value of the sawtooth-wave winding function
ϕ	Mechanical angle along the air-gap peripheral	i_{pm}	Fictionary current due to PM considering one turn
ϕ_0	Initial position from the reference axis	L_{xx}	Generalized form of inductance
h, n, r, and t	Positive integer representation of harmonics	Ψ_{abc-pm}, Ψ_{pm}	Simplified form of three-phase flux linkages and PM flux linkages
N_r	Number of rotor protrusions	i_{abc}, v_{abc}	Simplified form of three-phase winding currents and terminal voltages
ω_r	Mechanical rotor speed	$i_d^e, i_q^e, v_d^e, v_q^e$	Currents and voltages in synchronous frame
θ_{r0} and θ_r	Initial and current rotor positions	L_d^e, L_q^e	Inductances in synchronous frame

direct cooling methods [13], [14], [15], [16]. Thus, the risk of demagnetization of PMs in the proposed special machine can be alleviated significantly compared to rotor-bound PM-assisted synchronous reluctance motor.

The motor double salient special topology and the principles of operation have been described, together with the design optimization of a very high-power density prototype for EV traction, in a previous paper [1] and a dissertation [17] by the same group of authors. The current follow-up paper further expands the study by introducing a DQ motor model to enable vector control, and by describing prototyping and additional simulations and experimentation, including equivalent circuit parameter identification and separation of losses.

The stator of the studied electric machine includes 12 modules of concentrated coils in toroidal shape, which were separated by permanent magnets of opposite polarity inserted in the core, and a rotor with a castellated core structure. This topology was designed to have three phases, 4 coils per phase, 12 PMs, and a 10-pole reluctance type rotor with double saliency. Exploded view of the assembled motor and typical flux density were shown in Fig. 1 and 2.

An open frame lab prototype (OFLP) with air cooling and an experimental dyno test bench setup were developed. An equivalent circuit for the proposed special double salient machine was introduced with proper justification by implementing a minimum number of tests. These tests were open circuit test at rated speed, static torque test or locked rotor test at rated current to characterize the torque versus rotor positions, and unity power factor test as an uncontrolled generator to calculate the parameters. The preliminary results from these tests have been justified in this paper to establish an equivalent circuit by applying synchronous reference frame theory. In addition to these tests, 3D and 2D FEA simulations have been performed at identical operating points of the UPF test to numerically separate the loss components associated

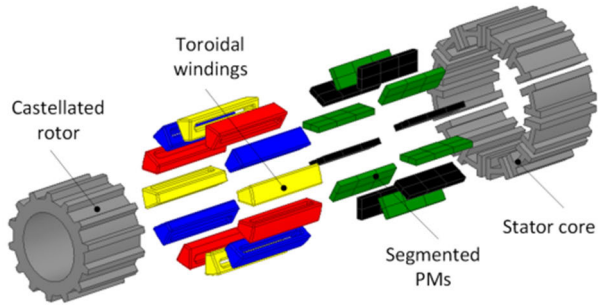

FIGURE 1. Exploded view of the proposed PM motor. The PM-free castellated rotor, modular stator, segmented PMs, and concentrated toroidal windings were the key features.

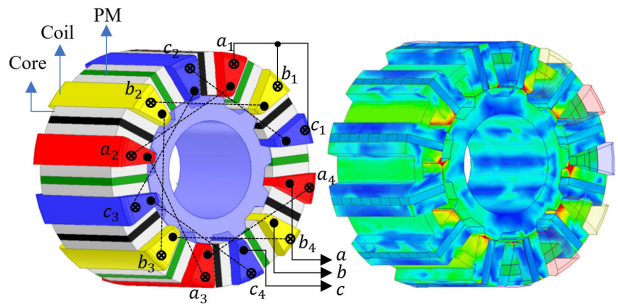

FIGURE 2. Model for 3D FEA and example magnetic field distribution for generator operation of the three-phase special modular machine with 12 concentrated coils and 12 PM in the stator. The reluctance rotor has 10 core protrusions, equivalent to a 20 consequent magnetic pole arrangement.

with the core, PMs, and coils of the special double salient machine.

An open frame lab prototype (OFLP) with air cooling and an experimental dyno test bench setup were developed. An equivalent circuit for the proposed special double salient machine was introduced with proper justification by implementing a minimum number of tests. These tests were open circuit test at rated speed, static torque test or locked rotor test at rated current to characterize the torque versus rotor

positions, and unity power factor test as an uncontrolled generator to calculate the parameters. The preliminary results from these tests have been justified in this paper to establish an equivalent circuit by applying synchronous reference frame theory. In addition to these tests, 3D and 2D FEA simulations have been performed at identical operating points of the UPF test to numerically separate the loss components associated with the core, PMs, and coils of the special double salient machine.

II. THEORY AND PRINCIPLE OF OPERATION

The principle of operation and production of torque for the proposed motor were discussed in this section. PM field and armature fields have been analyzed independently by considering an MMF-permeance model and winding functions as shown in Fig. 3. Nomenclature listed in table.1. was used in this paper.

Considering no slotting effect of stator core, the airgap flux density distribution due to PMs alone with no armature windings in the slots was expressed as (1). Likewise, the airgap flux density distribution due to armature winding alone has been expressed as (2). As per principle of virtual work, the electromagnetic torque was expressed as closed-form analytical airgap flux density distribution in (3).

$$\begin{aligned} B_{PM}(\phi,t) &= \frac{F_{PM}}{2h+1}\left\{\left(\frac{\Lambda_{max}+\Lambda_{min}}{2}\right)\sin\left[(2h+1)p_m(\phi-\phi_0)\right]\right. \\ &+\left(\frac{\Lambda_{max}-\Lambda_{min}}{4}\right)\sin\left[(2h+1)p_m+N_r\right] \\ &\cdot\left[\phi-\frac{N_r\omega_r}{(2h+1)p_m+N_r}t-\frac{(2h+1)p_m\phi_0+N_r\theta_{r0}}{(2h+1)p_m+N_r}\right] \\ &+\left(\frac{\Lambda_{max}-\Lambda_{min}}{4}\right)\sin\left[(2h+1)p_m-N_r\right] \\ &\left.\cdot\left[\phi-\frac{-N_r\omega_r}{(2h+1)p_m-N_r}t-\frac{(2h+1)p_m\phi_0-N_r\theta_{r0}}{(2h+1)p_m-N_r}\right]\right\} \end{aligned} \tag{1}$$

$$\begin{aligned} B_{AR}(\phi,t) &= \frac{3W_{max}I_m}{\pi}\left\{\left(\frac{\Lambda_{max}+\Lambda_{min}}{2}\right)\sum_{n=3r+1=tp_a}^{+\infty}\frac{1}{(n/p_a)}\right. \\ &\times\sin n\left[\phi-\left(\frac{\omega}{n}\right)t-\left(\phi_{a0}-\frac{\varphi_a}{n}\right)\right] \\ &+\left(\frac{\Lambda_{max}-\Lambda_{min}}{4}\right)\sum_{n=3r+1=tp_a}^{+\infty}\frac{1}{(n/p_a)}\sin(n+N_r) \\ &\times\left[\phi-\left(\frac{\omega-N_r\omega_r}{n+N_r}\right)t-\left(\frac{n\phi_{a0}+N_r\theta_{r0}-\varphi_a}{n+N_r}\right)\right] \\ &+\left(\frac{\Lambda_{max}-\Lambda_{min}}{4}\right)\sum_{n=3r+1=tp_a}^{+\infty}\frac{1}{(n/p_a)}\sin(n-N_r) \\ &\left.\times\left[\phi-\left(\frac{\omega+N_r\omega_r}{n-N_r}\right)t-\left(\frac{n\phi_{a0}-N_r\theta_{r0}-\varphi_a}{n-N_r}\right)\right]\right\} \end{aligned} \tag{2}$$

$$T_{em} = \frac{\partial W_{co}}{\partial\theta_r} = \frac{\partial}{\partial\theta_r}\int_V\frac{\{B_{PM}(\phi,t)+B_{AR}(\phi,t)\}^2}{2\mu_0}dv \tag{3}$$

As per (1), considering PMs as the only source, there exists three groups of flux density harmonics, with pole pairs $(2h+1)p_m$, $(2h+1)p_m+N_r$, and , $|(2h+1)p_m-N_r|$. Similarly, another three groups of flux density harmonics exist due to armature winding as the only source, with pole pairs $n=3r+1=tp_a$, $n+N_r$, and $|n-N_r|$. Furthermore, these harmonics were rotating at different speeds. By applying orthogonality relations of sine functions to (3), it can be inferred that only the flux density harmonics from PM field and armature field with same pole pairs will produce the non-zero average torque. Thus, the average electromagnetic torque of this motor was produced by multiple dominating air-gap flux density harmonics with pole pairs of 4, 6, 8, 16, 18 and 28.

It has been observed that there exists no torque in the absence of either of PMs in stator or current in the stator toroidal coils or protrusions in the rotor. Thus, the castellated rotor serves mainly as a modulator to couple armature winding and PMs through air-gap flux density harmonics. Another key observation has also revealed that there was no synchronous type reluctance torque despite the saliency due to protrusions in the rotor, which was proportional to product of d-axis and q-axis currents as in traditional synchronous machines.

Furthermore, the proper combinations of stator PMs, rotor poles, and stator winding modules producing non-zero average torques can be easily identified by observing the terms in (3). Many topologies can be derived from this approach. Typical topologies were 5-protrusion (5-P) and 7 protrusion (7-P) designs for a stator with 6 PMs and 6 toroidal coils, and 10-protrusion (10-P) and 14-protrusion (14-P) designs for a stator with 12 PMs and 12 toroidal coils.

Principle of operation and torque production of the proposed motor were explained by (1)-(3). However, these equations were not suitable to compute torque precisely. Thus, the Maxwell stress tensor method was used to compute radial and tangential components f_r and f_t of the electromagnetic stress in the airgap as expressed in (4) and (5).

$$f_r(\boldsymbol{\phi},\mathbf{t}) = \frac{B_r(\phi,t)^2-B_t(\phi,t)^2}{\mu_0} \tag{4}$$

$$f_r(\phi,t) = \frac{B_r(\phi,t)B_t(\phi,t)}{\mu_0} \tag{5}$$

The radial and tangential components of the force on stator teeth and rotor protrusions can be obtained by integrating the respective stress component over volumetric circumferential intervals. Computation of these stresses has been shown by an example in Fig. 4 and Fig. 5. Radial component of force density was significantly higher than tangential component. At any given position, radial force from two stator teeth of adjacent segments separated by magnet has been shown in Fig. 6. Torque contribution by these two stator teeth of

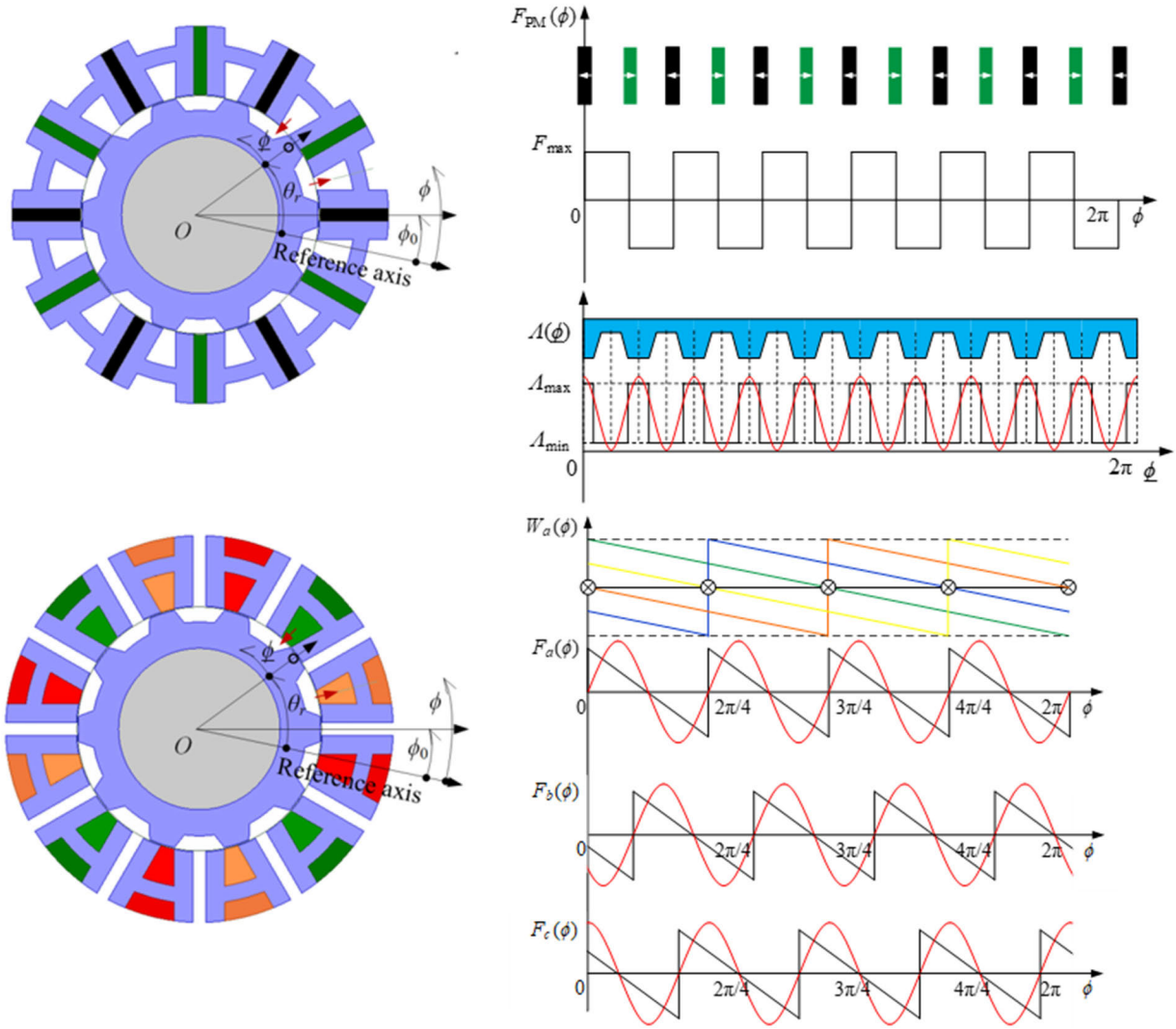

FIGURE 3. Schematics for motor cross section (left), and MMF-permeance motor models considering the PMs only (top right) and the armature windings only, respectively. The fundamental components of the air-gap permeance function and winding functions of armature coils were used for derivation. The winding functions of the toroidal windings were sawtooth waves, which were very different from the conventional slot windings.

adjacent segments separated by magnets was different from each other, but half symmetry has been observed as shown in Fig. 7. This approach was more feasible to calculate average torque contributed by stator teeth, magnets, and coils. Majority of the torque was produced by the leading teeth next to the magnet on left-hand side when looking into the page. Torque produced by the other teeth and magnet nearly cancel each other. The toroidal coils contribute almost no torque.

III. MULTI-OBJECTIVE DESIGN OPTIMIZATION BASED ON 2D FEA

Parametric models for a number of motor topologies were developed following the derived combinations from Section III. Based on the parametric electromagnetic FEA models for the 5-P, 7-P, 10-P and 14-P designs illustrated in Fig. 2 with 10 independent geometric and control variables,

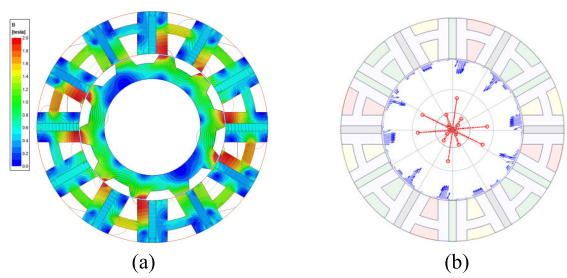

FIGURE 4. FEA results of the proposed motor at rated load, (a) flux density distribution and flux pattern, (b) electromagnetic force on stator teeth. Blue arrows denote the distributed force vectors and red dots denote the resultant forces on teeth.

a large-scale design optimization was performed, following the optimization approach used in, for example, [18] and [19]. The objective was to maximize the power density with

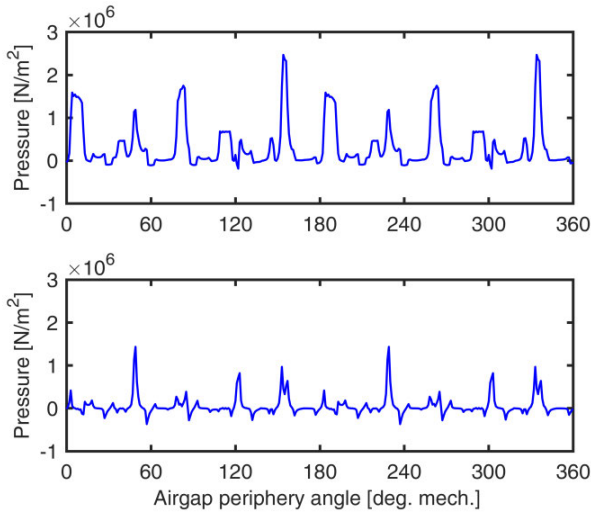

FIGURE 5. Air-gap stresses at rated load: radial component (top), (b) tangential component (bottom).

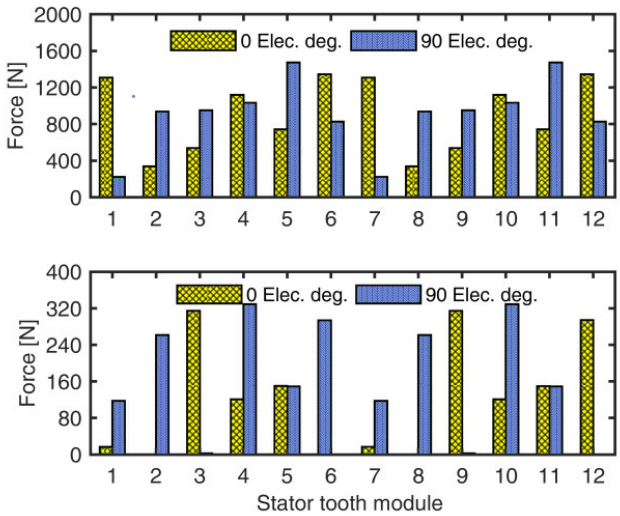

FIGURE 6. Radial (top) and tangential (bottom) force on the stator tooth module at different rotor position under rated load.

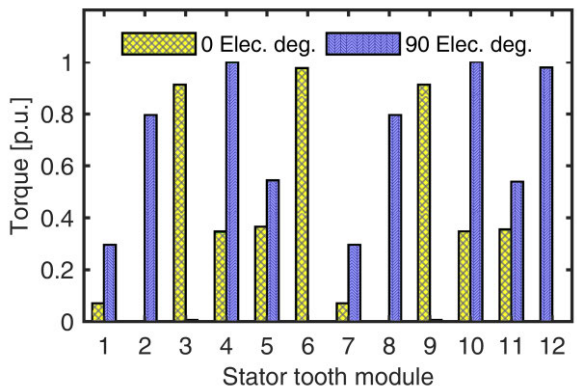

FIGURE 7. Radial (top) and tangential (bottom) force on the stator tooth module at different rotor position under rated load.

a 50kW/L target, efficiency, and power factor, assuming an equivalent electric loading, i.e., the product of current density and copper slot fill factor, equal to 9.75A/mm2 can

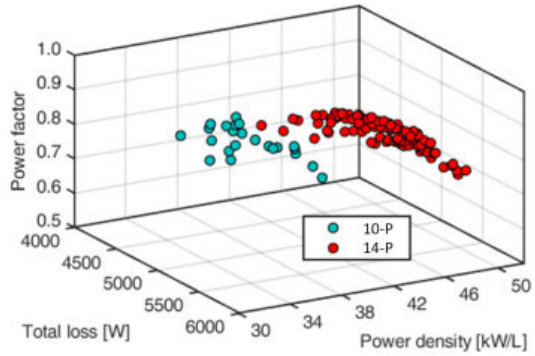

FIGURE 8. Optimization results: 3D Pareto front projection with objectives of total loss, power density, and power factor.

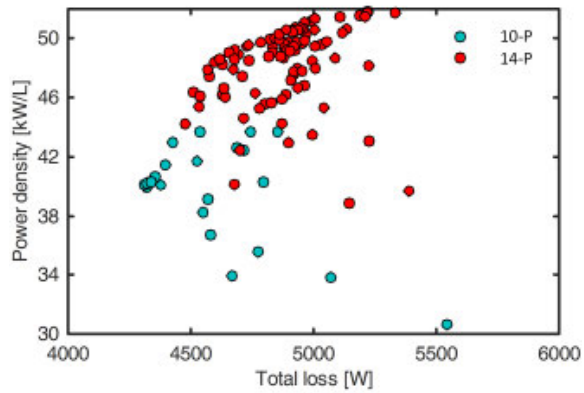

FIGURE 9. Optimization results projection in total loss - power density plane.

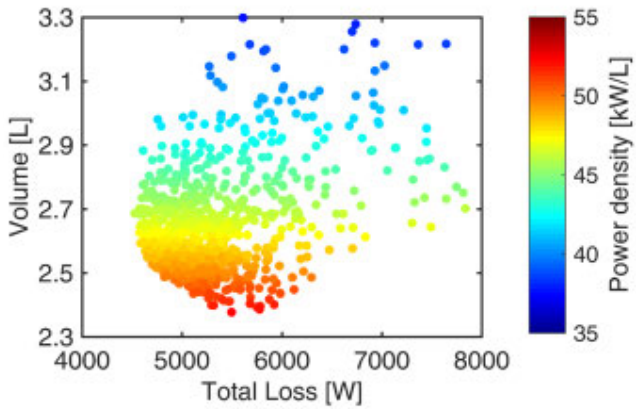

FIGURE 10. Optimization results: Pareto front of total loss and volume.

be achieved by the cooling design and advanced winding technology. The results of optimization studies indicated that specific torque increases with number of rotor protrusions, and so do core losses, in line with expectations.

A systematic comparative study between two motor topologies was also carried out based on multi-objective design optimizations, one with 10-P and the other 14-P, as shown in Fig. 8. The three concurrent objectives were to maximize the power density, minimize the total loss, and

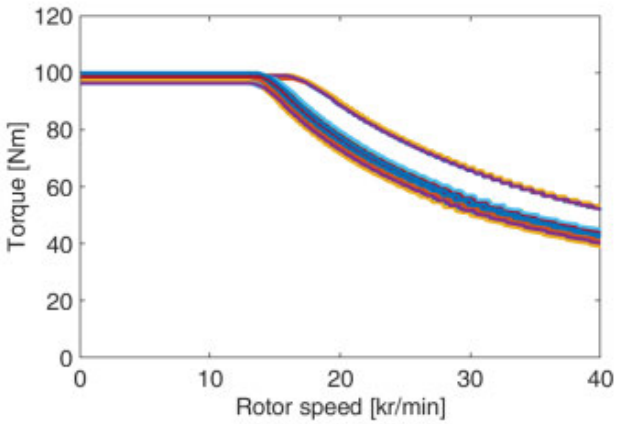

FIGURE 11. Torque-speed envelops of the Pareto front designs.

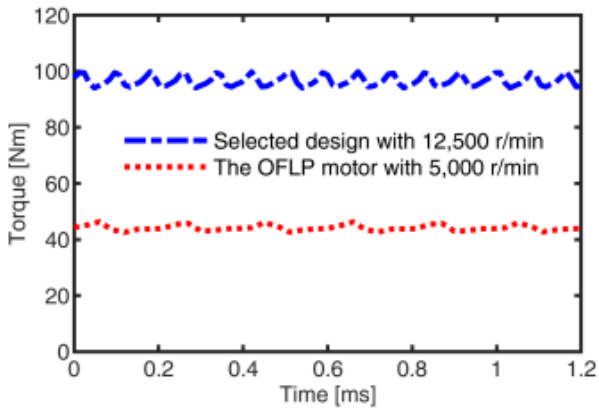

FIGURE 12. Torque waveform for high power density optimal design and its OFLP version. Low torque ripple was observed for both operation points.

maximize the power factor. The computational results show that, the optimal 14-P designs can achieve similar fundamental power factors as optimal 10-P designs. There were trade-offs between 10-P and 14-P designs in terms of the power density and total loss (Fig. 9).

Multiple design generations of the adopted differential evolution optimization yielded a satisfactory Pareto front. A number of candidate designs were identified, with estimated power density $\geq$ 50kW/L, as shown in Fig. 10. The torque speed and efficiency maps have also been calculated based on 2D electromagnetic FEA, as plotted in Fig. 11, showing that the optimally designed motor can operate with a constant power of 125kW at up to 3 times the base speed, which was 12,500r/min. The selected optimal design for the proposed topology produces 96Nm at 12,500r/min. The waveform of the OFLP motor and the optimal design can be seen Fig. 12.

IV. EXPERIMENTAL VALIDATION, JUSTIFICATION AND FORMULATION OF A DQ MODEL

To validate the proposed very high power density motor and the adopted design optimization approaches, as well as to

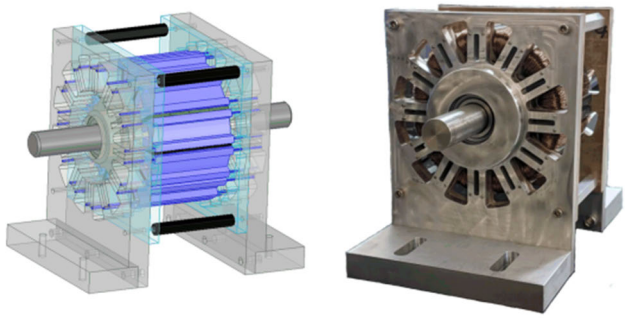

FIGURE 13. The CAD drawing and photo of the full assembly for the open frame lab prototype motor. Dowel pins were used in the laminated stator segments. PMs were segmented in both radial and axial directions to reduce the PM eddy current losses. All the coil terminals have been brought out for detailed testing purpose.

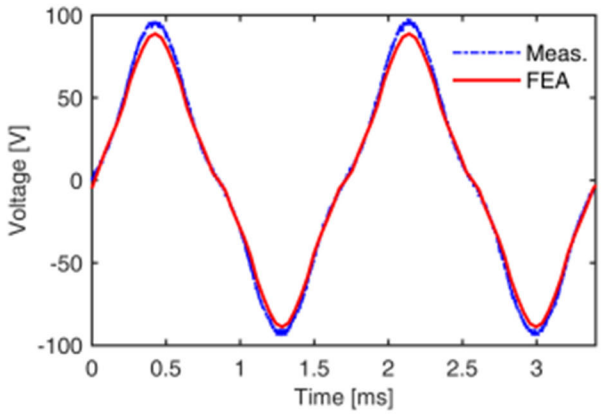

(a)

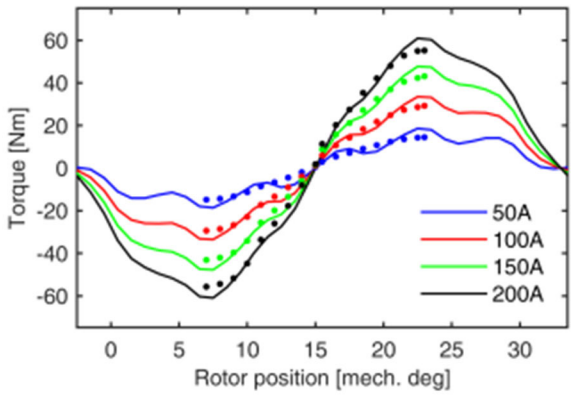

(b)

FIGURE 14. (a). Test and back EMF under open-circuit generator operation at 3525 rpm. (b). Test and FEA simulation results for static torque versus rotor position.

identify the potential challenges in manufacturing and testing to achieve the final goal of 50kW/L, a 28hp OFLP motor rated at 40Nm and 5,000r/min was fabricated, as shown in Fig. 13, and tested. An open circuit test on the OFLP has been performed at a rated speed of dyno test bench setup to identify the shape of the back EMF. A sinusoidal back EMF with low harmonics has been observed at the output terminal of the OFLP in both experimental test and FEA simulation as

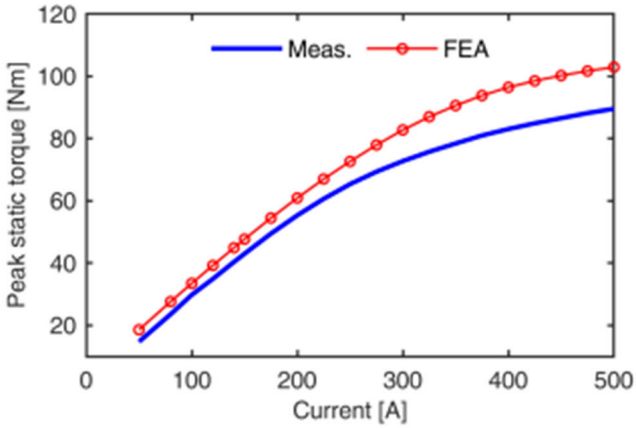

FIGURE 15. Testing and simulation results of peak torque versus different current values.

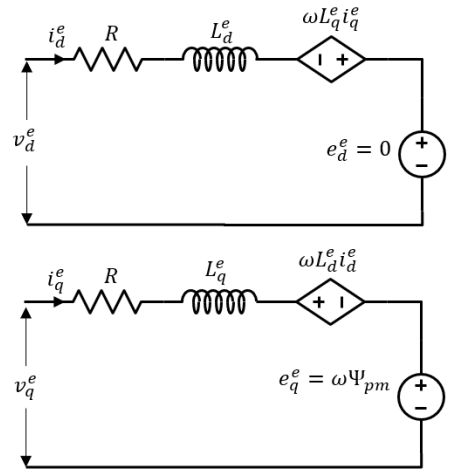

FIGURE 16. Schematic of the equivalent circuit of the proposed special machine in the synchronous reference frame.

TABLE 2. Experimental data from a unity power factor generator test, employed for inductance identification. The average inductance value satisfactorily compares with the value estimated based on FEA simulations.

Speed (RPM)	3500	3000	2400	2000
Frequency (Hz)	588	499	400	332
Load Current (A)	65	60	52	45
Terminal voltage per phase: V_a(V)	41.3	36.12	29.9	27.76
Induced voltage per phase: E_a (V)	52.3	43.6	34.8	30.1
Reactance per phase: $X_s = X_d = X_q$ (Ω)	0.493	0.406	0.324	0.264
Inductance per phase $L_s = L_d = L_q$ (μH)	133.61	129.80	129.18	126.68

shown in Fig. 14. (a). and Fig. 14. (b). A static torque test at a rated current of the OFLP has been implemented to plot the torque versus rotor positions. The torque of the OFLP has a peak at **90**° electrical as shown in Fig. 14. (b).

The static torques at different rotor positions were also measured when the phase-A winding was connected in series with the parallel of phase-B and phase-C windings. Each phase has 4 coils connected in series. It is shown that, within the expectation, the measured static torque has the same trend as the 2D FEA as seen in Figs 14.(a) and 15. The effect of magnetic saturation was captured precisely, which is significant for high current loading. The deviation is approx. 10% and can be explained by the backlash of the locking device, especially at the high torque region, the temperature rise, the inaccuracies of material properties, etc.

It was observed that there was no reluctance torque component present either in the experimental static torque test or FEA simulations. Thus, the special double salient machine can be modeled as a non-salient DQ model based on the results from the open-circuit test and static torque test. The speed and torque control strategies for the proposed special double salient machine can be established by applying synchronous reference frame theory to realize vector control. Thus, a DQ equivalent circuit of the proposed special machine has been realized in this paper. From the theory of doubly salient PM motor (DSPM) in [20], a generalized three-phase instantaneous torque was expressed as in (6). Equation (6) was a generic form of the three-phase instantaneous torque consisting of the magnetic and cogging torque components.

$$T = \left(i_a i_{pm}\frac{\partial L_{a-pm}}{\partial \phi} + i_b i_{pm}\frac{\partial L_{b-pm}}{\partial \phi} + i_c i_{pm}\frac{\partial L_{c-pm}}{\partial \phi}\right) + \frac{1}{2} i_{pm}^2 \frac{\partial L_{pm}}{\partial \phi} \tag{6}$$

The flux lines from the permanent magnets between the modular coils in the stator link with three-phase winding through a low reluctance path offered by the rotor. Thus, the flux linkages due to permanent magnets were a function of the rotor position as expressed in equation (7). The total flux linkages with the three-phase windings were due to the three-phase currents and permanent magnets were expressed as in equation (8).

Thus, the three-phase voltages were expressed as a rate of change of total flux linkages, in addition to the voltage drop due to the winding resistance as expressed in equation (9). The three-phase voltages were transformed into the synchronous frame by applying Clarke's transformation and Park's transformation to establish the expression (10). By neglecting the winding resistance and assuming the rate of change in the currents in (10) as negligible under steady-state conditions, the output power and torque were expressed as in equations (11) and (12). An equivalent circuit of the proposed special machine has been realized from the expression (10) was shown in Fig. 16. The speed and torque control strategies were required to be realized by considering the effect of nonlinearity, employing the look-up table method which will be discussed in subsequent work.

$$[\Psi_{abc-pm}] = \begin{bmatrix} \Psi_{a-pm} \\ \Psi_{b-pm} \\ \Psi_{c-pm} \end{bmatrix} = \begin{bmatrix} \cos\theta_r \\ \cos\left(\theta_r - \frac{2\pi}{3}\right) \\ \cos\left(\theta_r + \frac{2\pi}{3}\right) \end{bmatrix} \Psi_{pm} \tag{7}$$

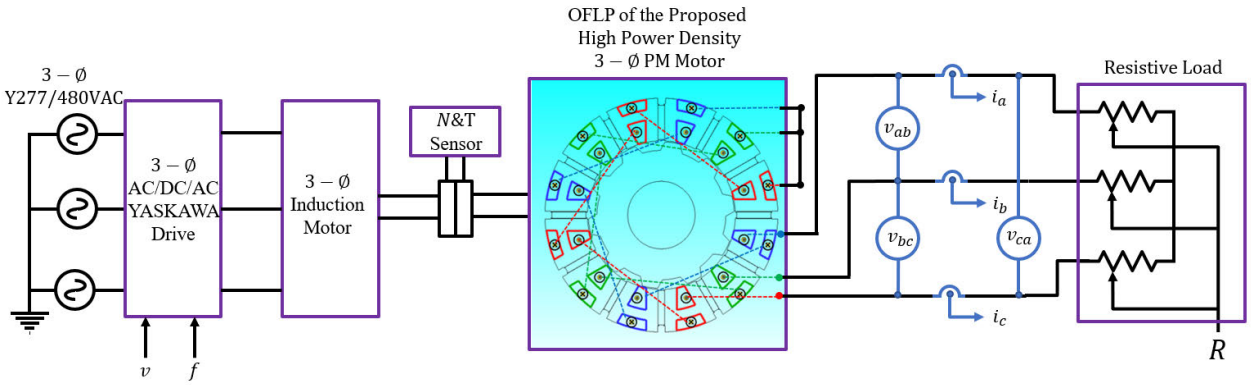

FIGURE 17. Schematic of the experimental dyno test setup of the OFLP of the proposed special double salient machine operating as a generator at unity power factor.

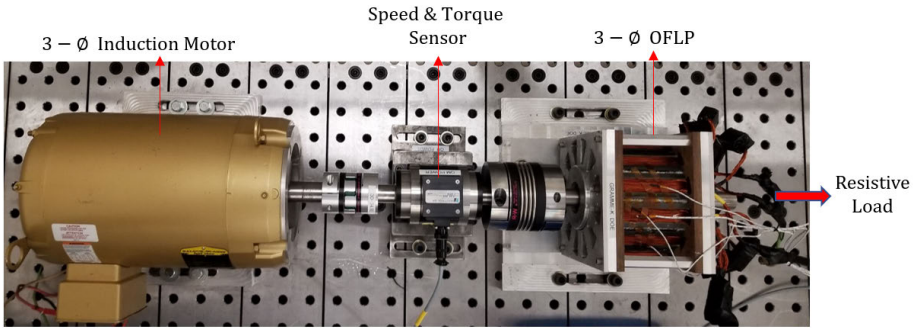

FIGURE 18. Picture of the experimental dyno test setup of the OFLP of the proposed special double salient machine operating as a generator at unity power factor.

$$\lambda_{total} = \begin{bmatrix} L_{aa} & L_{ab} & L_{ac} \\ L_{ba} & L_{bb} & L_{bc} \\ L_{ca} & L_{cb} & L_{cc} \end{bmatrix} \begin{bmatrix} i_a \\ i_b \\ i_c \end{bmatrix} + \begin{bmatrix} \Psi_{a-pm} \\ \Psi_{b-pm} \\ \Psi_{c-pm} \end{bmatrix} = [L_{abc}]\,[i_{abc}] + \left[\Psi_{abc-pm}\right] \tag{8}$$

$$[v_{abc}] = R\,[i_{abc}] + \frac{d}{dt}\left([L_{abc}]\,[i_{abc}] + \left[\Psi_{abc-pm}\right]\right) \tag{9}$$

$$\begin{bmatrix} v_d^e \\ v_q^e \end{bmatrix} = \begin{bmatrix} R & 0 \\ 0 & R \end{bmatrix} \begin{bmatrix} i_d^e \\ i_q^e \end{bmatrix} + \begin{bmatrix} L_d^e & 0 \\ 0 & L_q^e \end{bmatrix} \frac{d}{dt} \begin{bmatrix} i_d^e \\ i_q^e \end{bmatrix} + \begin{bmatrix} 0 & -\omega L_q^e \\ \omega L_d^e & 0 \end{bmatrix} \begin{bmatrix} i_d^e \\ i_q^e \end{bmatrix} + \begin{bmatrix} 0 \\ \omega \end{bmatrix} \Psi_{pm} \tag{10}$$

$$P_o = \frac{3}{2}\left[v_d^e \;\; v_q^e\right] \begin{bmatrix} i_d^e \\ i_q^e \end{bmatrix} = \frac{3}{2}\omega\left(i_d^e i_q^e\left(L_d^e - L_q^e\right) + \Psi_{pm} i_q^e\right) \tag{11}$$

$$T_{em} = \frac{P_o}{\omega_m} = \frac{3}{2}P\left(i_d^e i_q^e\left(L_d^e - L_q^e\right) + \Psi_{pm} i_q^e\right) \approx \frac{3}{2}P\Psi_{pm} i_q^e \tag{12}$$

V. EXPERIMENTAL AND NUMERICAL IDENTIFICATION OF EQUIVALENT DQ CIRCUIT PARAMETERS AND POWER LOSS COMPONENTS

An experimental test setup was developed to evaluate the inductance and losses for the proposed high-power density PM motor as shown in Fig. 17. The experimental setup consists of a three-phase AC/DC/AC drive, a three-phase induction motor, the OFLP of the proposed special machine, and a three-phase resistive load has been shown in Fig. 18. The UPF test has been implemented by operating the OFLP as a three-phase generator supplying power to a variable resistive load. The OLFP has been designed to run at a rated speed of 5000RPM at 41Nm.

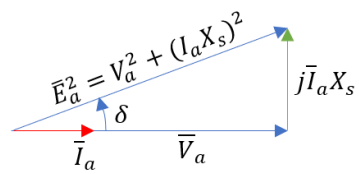

FIGURE 19. Schematic of per phase vector diagram of the OFLP as a generator driving a resistive load at unity power factor.

The three-phase induction motor was being used as a prime mover has a rated speed of 3525RPM at a load of 30Nm. A speed & torque sensor coupler has been mounted between the prime mover and OFLP. The line-to-line voltages and three-phase currents were measured at the output terminal of the OFLP. The OFLP has been operated at four different speeds at variable loads of up to 30Nm. The experimental results have been used to determine the inductance and to evaluate the losses. The experimental data of induced emf, terminal voltage, and load current at different operating points have been used to plot the per phase vector diagram and to determine inductance as shown in Fig. 19 and reported in table 2.

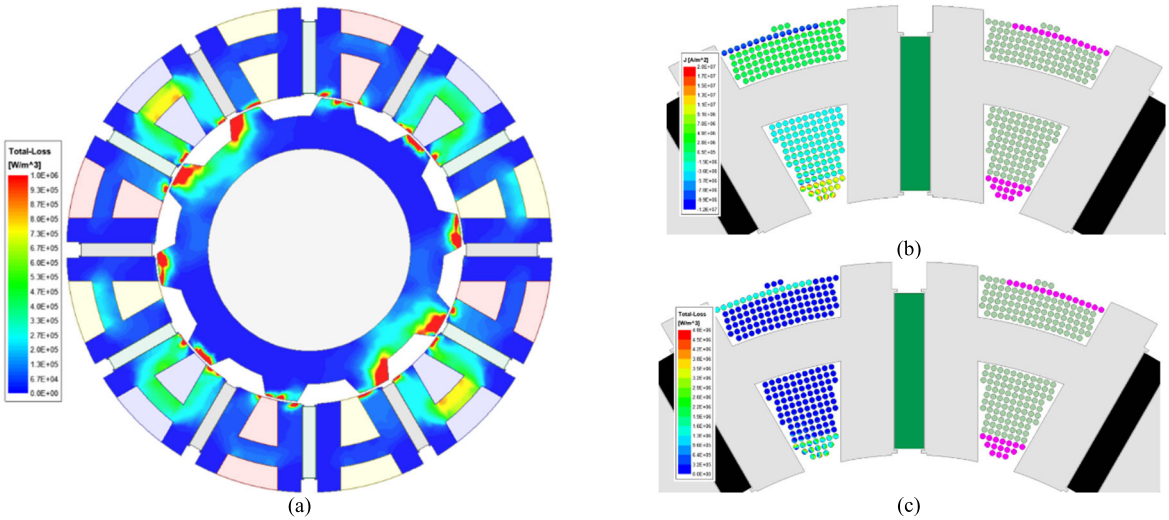

FIGURE 20. Electromagnetic 2D FEA results in the motor cross section. (a) Specific power losses in the stator and rotor laminated core (b) Eddy currents and (c) their associated power losses considering the details of the prototype winding.

TABLE 3. Experimental results and loss components calculated by 2D and 3D FEA.

Operating Points		Experimental Test Results			FEA 2D Simulation Results		FEA 3D Simulation Results	
Speed [RPM]	Current [A]	T_m [Nm]	P_{load} [W]	Joule Losses/Wdg. Cu Losses [W]	T_e [Nm]	Wdg. Eddy Current Losses [W]	Core Losses [W]	PM Losses [W]
3500	65	26.7	8075	191	30.5	171	282	50
3000	60	25.3	6988	163	28.3	143	212	35
2400	52	21.8	4652	121	24.5	102	144	22
2000	45	20	3657	92	21.4	75	105	14

Electromagnetic FEA simulations for this type of generator operation at 3,500 rpm and 65A resulted in an induced voltage of 53.7V and, though combinations with open-circuit simulations, to an inductance of 130.2uH, indicating satisfactory agreement with measurements.

The 2D and 3D FEA simulations for the special machine have been performed at the identical operating points of the experimental tests to numerically separate the losses providing a basis for the ongoing optimization studies. The 3D FEA schematic of the special double salient machine was shown in the Fig. 2. The 2D FEA schematic of the special double salient machine showing the eddy current losses and copper losses was shown in Fig. 20. Based on the practical availability in the laboratory settings, the winding has been prototyped with many parallel wires, i.e. "strands in hand". The top turns of the coils, which are closer to the airgap and are identified in red in the Fig. 20, experience the highest eddy current losses, as expected. These losses could be further reduced using thinner wire and advanced winding technology, as employed for high volume manufacturing.

A hybrid approach such as observations from the experimental tests and 3D and 2D FEA simulations were used

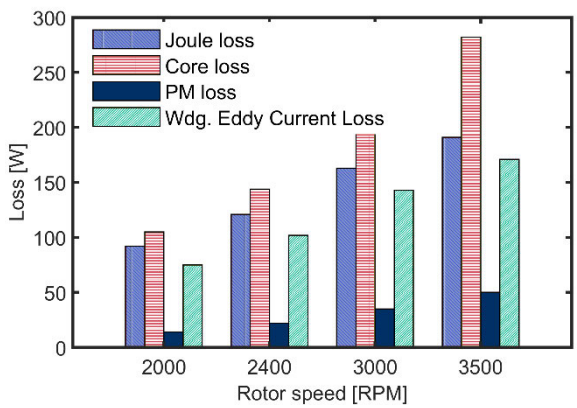

FIGURE 21. Loss components calculated by 3D and 2D FEA.

to determine the loss components. The 3D FEA simulations have been performed to evaluate the core losses associated with the rotor, stator, and eddy current losses in the PMs. 2D FEA simulations have been performed to determine the eddy current losses in the windings. Joule losses or copper losses of the winding were determined from the experimental test results. The conductors in the 2D schematic have

been arranged in a specific sequence of series and parallel combinations in identical with the winding structure of the OFLP. The conductors nearby stator core segments experience higher skin effect due to more flux linkages and hence higher inductance. Skin effect was less dominant in the conductors nearby airgap and hence distribution of current improves. The loss components at different operating points have been reported in table 3 and Fig. 21.

VI. CONCLUSION

The electric motor design proposed in this paper has multiple advantages, including topology suitable for enhanced direct coil cooling, construction for modular manufacturing, winding with separated phase coils and inherent fault tolerance, high-speed operation capability, and a wide speed range with a constant power speed ratio of at least 3:1. The optimal design study for electric vehicle traction applications indicates that very high-power density for the 50kW/L target may be indeed achieved provided that the electromagnetic configuration is supported by advanced winding technologies and effective cooling techniques.

The DQ frame model that has been established for the proposed machine and the equivalent circuit parameters identified through a minimum number of experimental tests indicate non-saliency characteristics with equal d and q inductances ($L_d = L_q$). The sinusoidal shape of the back EMF that has a very low harmonic content has been validated through open-circuit tests. Static torque tests at different current loadings and variable rotor position have shown no reluctance torque component, a characteristic specific to non-salient machines. Further parameter identification and power loss studies were performed on generator unity power factor tests. The results of the experimental observations and FEA simulations were in close agreement and provide a basis for ongoing optimization studies and vector control drive developments.

ACKNOWLEDGMENT

The material presented in this article do not necessarily reflect the views of the U.S. Department of Energy. The authors would like to gratefully acknowledge the direct support provided by QM Power Inc., and Ansys Inc.

REFERENCES

[1] P. Han, M. G. Kesgin, D. M. Ionel, R. Gosalia, N. Shah, C. J. Flynn, C. S. Goli, S. Essakiappan, and M. Manjrekar, "Design optimization of a very high power density motor with a reluctance rotor and a modular stator having PMs and toroidal windings," in *Proc. IEEE Energy Convers. Congr. Expo. (ECCE)*, Oct. 2021, pp. 4424–4430.

[2] *Electrical and Electronics Technical Road Map*, U.S. Drive Partnership, Oct. 2017.

[3] C. S. Goli, M. Manjrekar, S. Essakiappan, P. Sahu, and N. Shah, "Landscaping and review of traction motors for electric vehicle applications," in *Proc. IEEE Transp. Electrific. Conf. Expo (ITEC)*, Jun. 2021, pp. 162–168.

[4] C. S. Goli, S. Essakiappan, P. Sahu, M. Manjrekar, and N. Shah, "Review of recent trends in design of traction inverters for electric vehicle applications," in *Proc. IEEE 12th Int. Symp. Power Electron. Distrib. Gener. Syst. (PEDG)*, Jun. 2021, pp. 1–6.

[5] I. Husain, B. Ozpineci, M. S. Islam, E. Gurpinar, G.-J. Su, W. Yu, S. Chowdhury, L. Xue, D. Rahman, and R. Sahu, "Electric drive technology trends, challenges, and opportunities for future electric vehicles," *Proc. IEEE*, vol. 109, no. 6, pp. 1039–1059, Jun. 2021.

[6] C. J. Flynn, "Parallel magnetic circuit motor," Apr. 2011.

[7] C. J. Flynn, "Hybrid permanent magnet motor," Tech. Rep., Mar. 2011.

[8] Y. Liao, F. Liang, and T. A. Lipo, "A novel permanent magnet motor with doubly salient structure," *IEEE Trans. Ind. Appl.*, vol. 31, no. 5, pp. 1069–1078, Sep. 1995.

[9] R. P. Deodhar, S. Andersson, I. Boldea, and T. J. E. Miller, "The flux-reversal machine: A new brushless doubly-salient permanent-magnet machine," *IEEE Trans. Ind. Appl.*, vol. 33, no. 4, pp. 925–934, Jul. 1997.

[10] A. S. Thomas, Z. Q. Zhu, R. L. Owen, G. W. Jewell, and D. Howe, "Multiphase flux-switching permanent-magnet brushless machine for aerospace application," *IEEE Trans. Ind. Appl.*, vol. 45, no. 6, pp. 1971–1981, Sep. 2009.

[11] H. Chen, A. M. El-Refaie, and N. A. O. Demerdash, "Flux-switching permanent magnet machines: A review of opportunities and challenges—Part I: Fundamentals and topologies," *IEEE Trans. Energy Convers.*, vol. 35, no. 2, pp. 684–698, Jun. 2020.

[12] H. Chen, A. M. El-Refaie, and N. A. O. Demerdash, "Flux-switching permanent magnet machines: A review of opportunities and challenges—Part II: Design aspects, control, and emerging trends," *IEEE Trans. Energy Convers.*, vol. 35, no. 2, pp. 699–713, Jun. 2020.

[13] P. Lindh, I. Petrov, A. Jaatinen-Värri, A. Grönman, M. Martinez-Iturralde, M. Satrústegui, and J. Pyrhönen, "Direct liquid cooling method verified with an axial-flux permanent-magnet traction machine prototype," *IEEE Trans. Ind. Electron.*, vol. 64, no. 8, pp. 6086–6095, Aug. 2017.

[14] R. Camilleri, D. A. Howey, and M. D. McCulloch, "Predicting the temperature and flow distribution in a direct oil-cooled electrical machine with segmented stator," *IEEE Trans. Ind. Electron.*, vol. 63, no. 1, pp. 82–91, Jan. 2016.

[15] P. M. Lindh, I. Petrov, R. S. Semken, M. Niemelä, J. J. Pyrhönen, L. Aarniovuori, T. Vaimann, and A. Kallaste, "Direct liquid cooling in low-power electrical machines: Proof-of-concept," *IEEE Trans. Energy Convers.*, vol. 31, no. 4, pp. 1257–1266, Dec. 2016.

[16] R. Lehmann, M. Künzler, M. Moullion, and F. Gauterin, "Comparison of commonly used cooling concepts for electrical machines in automotive applications," *Machines*, vol. 10, no. 6, p. 442, Jun. 2022.

[17] M. G. Kesgin, "Optimal design of special high torque density electric machines based on electromagnetic FEA," M.S. thesis, Dept. Elect. Comput. Eng., 2023, p. 193.

[18] M. Rosu et al., *Multiphysics Simulation by Design for Electrical Machines Power Electronics and Drives*. Hoboken, NJ, USA: Wiley.

[19] V. Rallabandi, P. Han, J. Wu, A. M. Cramer, D. M. Ionel, and P. Zhou, "Design optimization and comparison of direct-drive outer-rotor SRMs based on fast current profile estimation and transient FEA," *IEEE Trans. Ind. Appl.*, vol. 57, no. 1, pp. 236–245, Jan. 2021.

[20] N. S. Lobo, "Doubly salient permanent magnet flux-reversal-free-stator switched reluctance machines," Ph.D. dissertation, Virginia Polytech. Inst., State Univ., Jan. 2011.

CHANDRA SEKHAR GOLI (Graduate Student Member, IEEE) received the B.E. degree in electrical and electronics engineering from Andhra University, India, in 2010, the M.Tech. degree in electrical and electronics engineering from the Visvesvaraya National Institute of Technology, Nagpur, India, in 2013, and the M.S. degree in electrical engineering from The University of North Carolina at Charlotte, USA, in 2022, where he is currently pursuing the Ph.D. degree. His electrical engineering research interests include electric machine design, power electronic drives, and control systems.

MURAT GURHAN KESGIN (Graduate Student Member, IEEE) received the M.Sc. and Ph.D. degrees in electrical engineering from the University of Kentucky, Lexington, KY, USA, in 2017 and 2023, respectively. He is currently a Senior Software Engineer with Conga, Broomfield, CO, USA. His research interests include programming languages, advanced electromagnetic FEA, electric machine design, optimization, and power electronic drives.

PENG HAN (Senior Member, IEEE) received the B.Sc. and Ph.D. degrees in electrical engineering from the School of Electrical Engineering, Southeast University, Nanjing, China, in 2012 and 2017, respectively. From November 2014 to November 2015, he was a joint Ph.D. Student with the Department of Energy Technology, Aalborg University, Aalborg, Denmark, where he focused on the brushless doubly-fed machines for wind energy conversion and high power drive, funded by the China Scholarship Council. He was a Postdoctoral Researcher with the Department of Electrical and Computer Engineering, Center for High Performance Power Electronics (CHPPE), The Ohio State University, and later the SPARK Laboratory, Department of Electrical and Computer Engineering, University of Kentucky. He is currently with Ansys Inc., as a Senior Application Engineer. His current research interests include electric machines, power electronics, and renewable energy.

DAN M. IONEL (Fellow, IEEE) received the M.Eng. and Ph.D. degrees in electrical engineering from the Polytechnic University of Bucharest, Bucharest, Romania. His doctoral program included a Leverhulme Visiting Fellowship with the University of Bath, Bath, U.K. He was a Postdoctoral Researcher with the SPEED Laboratory, University of Glasgow, Glasgow, U.K. He is currently a Professor of electrical engineering and the L. Stanley Pigman Chair in Power with the University of Kentucky, Lexington, KY, USA, where he is also the Director of the Power and Energy Institute of Kentucky and the SPARK Laboratory. Previously, he was with industry, most recently a Chief Engineer with Regal Beloit Corporation, Grafton, WI, USA, and before that, the Chief Scientist of Vestas Wind Turbines. He was also a Visiting Professor and a Research Professor with the University of Wisconsin and Marquette University, Milwaukee, WI. He has contributed to technology developments with long lasting industrial impact, holds more than 40 patents, and has authored or coauthored two books and more than 200 technical papers, including IEEE award winners. He was a recipient of the Cyril G. Veinott Award from the IEEE Power and Energy Society. He was the Inaugural Chair of the IEEE Industry Applications Society Renewable and Sustainable Energy Conversion Systems Committee. He was the Chair of the IEEE Power and Energy Society Electric Motor Subcommittee and the General Chair of the IEEE 2017 Anniversary Edition of the International Conference on Electrical Machines and Drives (IEMDC). He is currently the Chair of the IEEE IEMDC Steering Committee. He was an Editor of IEEE Transactions on Sustainable Energy.

SOMASUNDARAM ESSAKIAPPAN (Senior Member, IEEE) received the B.E. degree in electrical and electronics engineering from the College of Engineering Guindy, in 2007, and the M.S. and Ph.D. degrees in electrical engineering from Texas A&M University, in 2010 and 2014, respectively. He has been an Adjunct Professor with the Department of Electrical and Computer Engineering, The University of North Carolina at Charlotte, since 2015, where he is responsible for courses in power and leading sponsored research projects. Previously, he was an Research and Development Engineering Manager with QM Power Inc., responsible for leading programs on new motor architectures and motor drive development projects, from 2021 to 2023. Prior to that, he was a Teaching Professor and the Manager of the Flexible Energy Laboratories, Energy Production and Infrastructure Center, The University of North Carolina at Charlotte, from 2016 to 2021, where he has developed and managed a high-power research and industrial testing laboratory for power electronic systems. He has published about 50 research articles in various disciplines of power engineering. He is an inventor of two awarded U.S. patents and multiple pending patent applications. His research interests include power electronics for distributed energy integration, power quality and resiliency, and motors and drives.

He is an active volunteer in professional societies and serves as a member for the Power Electronics Society Magazine Advisory Board and a reviewer for major journals and conferences. In the past, he has served as the Chair for the Young Professionals of IEEE Power Electronics Society and the Technical Program Chair for the 9th and 12th editions of the International Symposium on Power Electronics for Distributed Generation Systems (PEDG).

JAMES GAFFORD (Senior Member, IEEE) is with the Energy Production and Infrastructure Center (EPIC), William States Lee College of Engineering, The University of North Carolina at Charlotte, as a Professor of Practice. His appointments include the EPIC Assistant Director of research for power management and the Director of special projects. He has more than 20 years of experience in research and development laboratories. His work includes the development of advanced power electronics and vehicle autonomy. His current research interests include wide bandgap semiconductor device applications, reliability and resiliency of critical power systems, integration distributed energy resources, predictive control systems, vehicle electrification, and the resultant impact on grid utility services.

MADHAV D. MANJREKAR (Senior Member, IEEE) was born in 1972. He received the B.E. degree from the Government College of Engineering, University of Pune, India, in 1993, the M.Tech. degree from the Center for Electronic Design and Technology, Indian Institute of Science, India, in 1995, the M.S. degree from Montana State University, Bozeman, in 1997, and the Ph.D. degree in electrical engineering from the University of Wisconsin, Madison, in 1999. From 2000 to 2005, he was an electrical engineer with power industry. He became an Assistant Professor of electrical engineering with The University of North Carolina (UNCC) at Charlotte, in 2005, where he is currently an Associate Professor with the Department of Electrical and Computer Engineering. He is also the Assistant Director of the Energy Production and Infrastructure Center (EPIC), which is a research center of energy, power, and power electronics.